Computers and Electronics in Agriculture 222 (2024) 109003

Contents lists available at ScienceDirect

Computers and Electronics in Agriculture

journal homepage: www.elsevier.com/locate/compag

Operational workflow to simulate biophysical variables, based on the coupled WRF/SEBAL models

Amirhossein Nikfal [a,*], Mohammad Amin Karimi [b]

[a] Jülich Supercomputing Centre (JSC), Forschungszentrum Jülich, Jülich, Germany
[b] SRIco (Soroosh Rayaneh Iranian), Tehran, Iran

ARTICLE INFO

Keywords:
Evapotranspiration
SEBAL
WRF
VIIRS
SENTINEL2

ABSTRACT

Three subsystems including an atmospheric regional forecast and analysis system, satellite data retrieval and processing, and a surface energy balance model have been employed in a 24/7 operational system to measure and simulate some primary agricultural variables, including evapotranspiration, biomass production, and other associated productivity metrics such as NDVI and Albedo. The final products are generated in a daily routine, covering Iran as the domain of simulation. The WRF atmospheric model, VIIRS, and SENTINEL2 satellite data, as well as the SEBAL model (implemented in pySEBAL) are the main components of the operational system, with products in two different spatial resolutions of 375 m and 100 m. The output products can be used by farmers and stakeholders to manage agricultural water requirements and monitor biophysical parameters.

1. Introduction

Proper water management in agriculture has a significant role in various sectors, such as the quality and quantity of biomass production and the monitoring of crop yield. This issue is even more imperative when it comes to the arid and semi-arid regions of West Asia and the Middle East. Over 90% of water consumption in Iran goes to agriculture. However, due to the low efficiency of irrigation, the crop yield is very low (Alizadeh and Keshavarz, 2005). According to Madani (2014), the average irrigation efficiency in Iran is less than 35% and only 5% of the cultivated areas are under mechanized pressured irrigation. This inefficiency in agricultural production and water management have been deteriorated over the past decades, due to the negative impacts of climate change (Karimi et al., 2018). Drought as one of the main consequences of climate change, imposes additional vulnerabilities in agricultural operations and economic insecurities for farmers (Zarafshani et al., 2012), as well as consumers.

There is a reciprocal relationship between agricultural production and water consumption with drought. Either one can impact the other. Drought can be calculated as an index of evapotranspiration (Tsakiris and Vangelis, 2005). Scarce water resources lead to low crop yield, and inefficient water consumption aggravates the drought, with adverse effects on sustainable agriculture (Theron et al., 2021). According to Lu et al. (2020), non-irrigated crops in comparison to irrigated ones, are more sensitive to drought, which strengthens the role of irrigation to mitigate the drought impacts on agriculture in the US. Crop yields are highly correlated with the Soil Moisture Deficit Index (SMDI) and Evapotranspiration Deficit Index (ETDI), which indicates that the aforementioned indices can be used to monitor agricultural drought (Narasimhan and Srinivasan, 2005). The representation of evapotranspiration (ET) and runoff processes in drought indices must be thoroughly considered, since they can have a paradoxical relationship with water storage anomalies (Teuling et al., 2013). It has been shown that large changes in potential ET can cause soil moisture deficit and vegetation scarcity; and due to the lack of realistic Land Surface Models, the increase of drought has been understated in most General Circulation Models (Rind et al., 1990).

Since evapotranspiration has considerable applications in water management (Goyal and Harmsen, 2013), ET simulation and its spatiotemporal variation are of primary concern in agricultural studies and policies. The simulated annual evapotranspiration from 1984 to 1997, over Lushi basin showed good agreement with precipitation minus discharge at the outlet, and the ET spatial pattern corresponded to those of the Leaf Area Index (LAI) over the study region (Mo et al., 2004). Several studies have been done to estimate evapotranspiration with different algorithms (Kool et al., 2014; Xiang et al., 2020; Zhang et al., 2016). The Satellite Application Facility on Land Surface Analysis (LSA SAF) provides a series of operational products from MSG-SEVIRI satellite sensors, including evapotranspiration. Comparison of two years of ET observations (2010–2011) with the ET simulations from LSA SAF (https://landsaf.ipma.pt/en/) have shown a pretty high correlation of 0.71 (Petropoulos et al., 2016). In another study over a region in Spain,

---

* Corresponding author.
E-mail address: a.nikfal@fz-juelich.de (A. Nikfal).

https://doi.org/10.1016/j.compag.2024.109003
Received 8 June 2023; Received in revised form 24 April 2024; Accepted 30 April 2024

the irrigation water requirement has been estimated using the soil–water–atmosphere–plant (SWAP) model and Landsat remote sensing images, with an interval of 15 days in the output data (Droogers et al., 2010).

One of the models that can employ remote sensing images to estimate evapotranspiration is the Surface Energy Balance Algorithm for Land (SEBAL) (Bastiaanssen et al., 1998a). The surface flux as the output of the SEBAL model has been validated with field data from some experiments in Spain, Niger, and China, indicating that in 85% of the cases, the differences were within the range of instrumental errors (Bastiaanssen et al., 1998b). Sensible and latent heat fluxes, associated with dry and wet pixels, have primary roles in the SEBAL model to estimate evapotranspiration. Tang et al. (2013) investigated the relationship between the satellite pixel sizes with the estimated ET by the SEBAL algorithm, as a function of some surface variables, such as near-surface air temperature and momentum roughness length. SEBAL algorithm has been employed in the estimation of the actual ET, using the Landsat −7 images, determining the open water bodies and swamps with the highest ET, cropland and grassland as the second highest ET, and bare soil with the lowest evapotranspiration (Sun et al., 2011).

Equations of evapotranspiration have been implemented in various software applications. One of the well known software tools in geoscientific applications is QGIS QGIS Development Team (2020). QWaterModel (Ellsäßer et al., 2020) is a QGIS plugin for predicting evapotranspiration from land surface temperature, based on the Deriving Atmosphere Turbulent Transport Useful To Dummies Using Temperature (DATTUTDUT) model. DATTUTDUT model limits the input requirements to solely land surface temperature (LST) information (Brenner et al., 2018). SEBALIGEE is another software application for the Google Earth Engine (GEE) to produce monthly evapotranspiration, which is based on the SEBAL-improved (SEBALI) model with Landsat −8 images (Mhawej and Faour, 2020). A carbon–water coupled model by integrating vapor pressure deficit and soil moisture into a stomatal conductance submodule to estimate forest carbon and water fluxes, is another application provided as an R package (rTRIPLEX-CWFlux) (Sun et al., 2023). The aforementioned SEBAL model is also implemented in Python, known as pySEBAL (Xue et al., 2020 and Caiserman et al., 2021), that has been used in this work as one of the three subsystems of the operational water management system.

The provision of atmospheric data in any field of study associated with environmental science is a key consideration. Agriculture as a multidisciplinary study is significantly affected by atmospheric variables. Therefore, the accuracy of atmospheric data directly impacts the accuracy of an agricultural management system. The Weather Research and Forecasting System, known as the WRF model (Skamarock et al., 2019) is a regional atmospheric model with multiple applications in environmental and agricultural science. The capability of high resolution atmospheric data simulated by the WRF model to investigate spatially distributed soil-moisture deficits in farmlands has been discussed by Hong et al. (2021). It has been shown that the bias-corrected WRF precipitation data could improve the predictability of the soil moisture deficit. The crop Evapotranspiration over a region of irrigated orchards has been simulated by the coupled WRF/ACASA models. The Advanced Canopy-atmosphere-soil Algorithm (ACASA) (Pyles, 2000) is a micrometeorological algorithm for the atmospheric surface layer and its associated variables. The results were consistent maps of evapotranspiration over an area of 1600 km^2, with a spatial resolution of 500 m (Falk et al., 2014).

Agricultural farms need continual warning advisory systems to cope with various severe weather phenomena, such as drought and frost, and strengthen their resilience. Such system as an operational workflow critically depends on atmospheric variables. In this article, the coupled WRF/SEBAL models have been employed to simulate the key agricultural variables of evapotranspiration and biomass, as well as other associated variables such as atmospheric temperature and LAI.

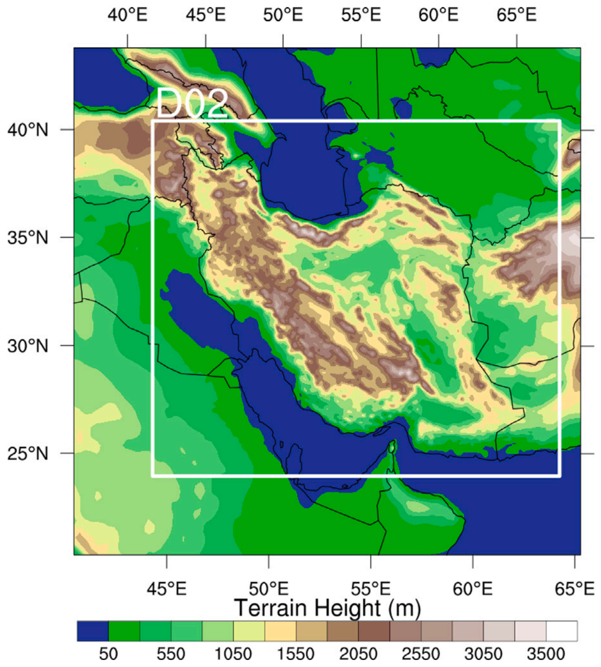

Fig. 1. WPS domain configuration. D02 as the WRF subdomain is the region of study.

2. Materials and methods

The SEBAL model has been employed in an operational workflow to simulate ET and other agrometeorological variables over the study region. SEBAL model requires various input variables, including atmospheric and remote sensing data. Some static data, consisting of soil and topography are also required. Atmospheric variables required to run the SEBAL model, are the most challenging data among all the input variables. Atmospheric data can be provided in 2 ways, either by using the global forecast model outputs or by direct regional simulations. For the sake of higher accuracy, we established an operational weather forecast system based on the WRF model to provide the atmospheric variables required to run the SEBAL model.

Fig. 1 shows the domain configurations for running the WRF model as the first stage of the water management operational system. D02 as the WRF subdomain represents the main region of study, covering the whole country of Iran.

2.1. Operational weather forecasting: WRF model

SEBAL model needs two types of temporally different atmospheric data: instantaneous, and daily averaged. The instantaneous atmospheric variables are required almost at the same time as the satellite overpass time on the study region (simulation domain). This might be possible if the meteorological station data can be immediately available after retrieving the satellite data. However, the average atmospheric variables cannot be provided in the middle of the day and close to the satellite overpass time, unless by using atmospheric forecast data. Some primary atmospheric variables are required as input data to the SEBAL model: 2 m temperature (C), relative humidity (%), wind speed (m s^{-1}), downward shortwave radiation (W m^{-2}), and air density (kg m^{-3}). The total number of atmospheric variables are much more than the aforementioned variables. However, by using the elevation data, they are being estimated at the final step of the operational system.

WRF model forecasts provide the required atmospheric variables in a uniform grid to cover the whole simulation domain. Spatial resolutions of the WRF simulation domains (Fig. 1), as well as other model configurations, are shown in Table 1. Atmospheric global data from

Table 1
WRF model configurations.

Parent-domain spatial resolution	30 km (90 × 90)
Nested-domain spatial resolution	10 km (214 × 187)
Pressure on top of atmosphere	50 h Pa (34 levels)
Run start time	12:00 UTC
Initialization data	NCEP GFS 0.5 degree
Physics suite	CONUS

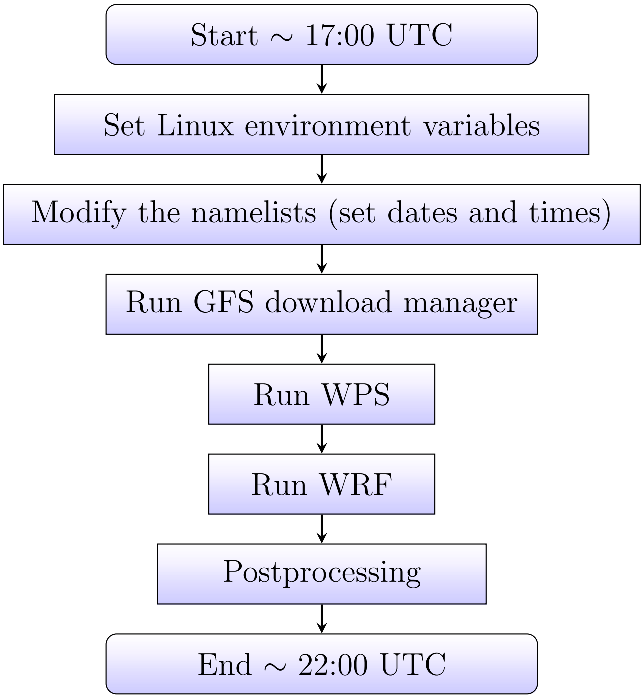

Fig. 2. Streamflow of the WRF operational forecast system.

the Global Forecast System (GFS) (https://nomads.ncep.noaa.gov/pub/data/nccf/com/gfs/prod/) have been used to initialize the WRF model and provide the atmospheric boundary conditions. GFS is a weather forecast model supported by the National Centers for Environmental Prediction (NCEP) that generates data for atmospheric and land-soil variables.

WRF model is set to make forecasts for the next day, so they can be ingested into the SEBAL model to simulate the agrometeorological variables. In other words, the atmospheric variables as the input data for each day, are the forecasts of the WRF model that was run on the day before. Fig. 2 shows the different stages in running the WRF model in a daily operational streamflow forecast system. A driver is installed as a cron job to run the WRF workflow starting at around 17:00 UTC every day. After running the WRF model, the output for the nested domain is postprocessed, consisting of 2 tasks: extracting the required atmospheric variables as instantaneous and averaged data; and converting them from NetCDF to GeoTIFF data. Therefore, they can be ingested into the final step in the SEBAL model. The instantaneous data are extracted from WRF outputs at around 11:00 UTC, which is close to the time of the Suomi-NPP satellite overpass on Iran as the region of study.

Fig. 3 shows some sample WRF outputs for the nested domain (region of study) as the input data for the SEBAL model, visualized by the PostWRF software tools (Nikfal, 2023).

2.2. Satellite data

Satellite data have a primary role in the SEBAL model to simulate evapotranspiration and other agrometeorological variables. Thermal infrared imagery, as well as those satellite bands required in calculating the Normalized Difference Vegetation Index (NDVI) and Albedo, are processed during the workflow. The Visible Infrared Imaging Radiometer Suite (VIIRS) (Cao et al., 2013) and SENTINEL2 (Drusch et al., 2012) images, as two different satellite data are retrieved, preprocessed, and postprocessed, before being ingested into the SEBAL calculations. The VIIRS data is exceptionally important, because it provides the thermal band, while the SENTINEL2 data have higher spatial resolution, but with no thermal band. The model is run in 2 different spatial resolutions. 375 m and 100 m. The 375 m products are all based on the VIIRS data. However, the 100 m products are based on SENTINEL2 data, with the exception of the thermal band which is the VIIRS thermal band (I5).

Table 2
VIIRS spectral bands used by the SEBAL model.

Band	Reflective range (μm)	Explanation	Spatial resolution
M2	0.436–0.454	Visible	750 m
I1	0.6–0.68	Visible	375 m
I2	0.85–0.88	NIR	375 m
I3	1.58–1.64	SWIR	375 m
I5	10.5–12.4	LWIR	375 m

2.2.1. VIIRS images

Characteristics of the VIIRS spectral bands are shown in Table 2. All calculations regarding the vegetation indices and land surface temperature are carried out by the SEBAL model, and not many postprocessing tasks are needed for the VIIRS data, once they are retrieved. Regarding Fig. 4, the start of the VIIRS workflow is the start of the SEBAL workflow. VIIRS data archive is available at https://nrt3.modaps.eosdis.nasa.gov/api/v2/content/archives/allData.

We desire only those images that cover the whole or part of the region of study. For this aim, the orbital period of the SUOMI satellite is calculated and the overpassing times in Iran are estimated. Therefore, at most, up to four files per day might be identified as the VIIRS images that cover Iran as the simulation domain. VIIRS real-time data are based on NetCDF, and after complete download, they are converted to GeoTIFF, to be ingested into the SEBAL model.

Most of the time, more than one VIIRS image covers the region of study (Iran). Therefore, in the case of multiple VIIRS images (Fig. 5), they are merged into one image. Since the temporal difference is at most around 1 h, it can be neglected in the final SEBAL simulation, and all merged images are considered to be at the same time. Eventually, as the final step in the VIIRS retrieval streamflow, VIIRS data are moved to a directory containing all input data needed to run the SEBAL model. VIIRS data at first were retrieved from the Suomi NPP satellite. However, after the end of the satellite mission life (June 2022), we replaced the previous Suomi-NPP VIIRS data with NOAA-20 VIIRS data, which is supposed to have a mission life until 2027. The final SEBAL products based on the VIIRS data have the same spatial resolution as the satellite data (375 m).

2.2.2. SENTINEL2 images

SENTINEL2 data are used in the second run of the SEBAL model to generate 100 m products. The vegetation indices of NDVI and Albedo are calculated out of these data, before running the SEBAL model as the input data for the final simulations. Regarding the first step of the flowchart in Fig. 6, retrieval of SENTINEL2 data starts after 7 h from the end of the first run of the SEBAL model and generating evapotranspiration and other 375 m agrometeorological products. This lag is necessary to ensure the sensed data is available in on the Copernicus Data Space Ecosystem (https://dataspace.copernicus.eu).

SENTINEL2 data are being downloaded as raw data format (SAFE). Eq. (1) shows the calculation of NDVI by the associated SENTINEL2

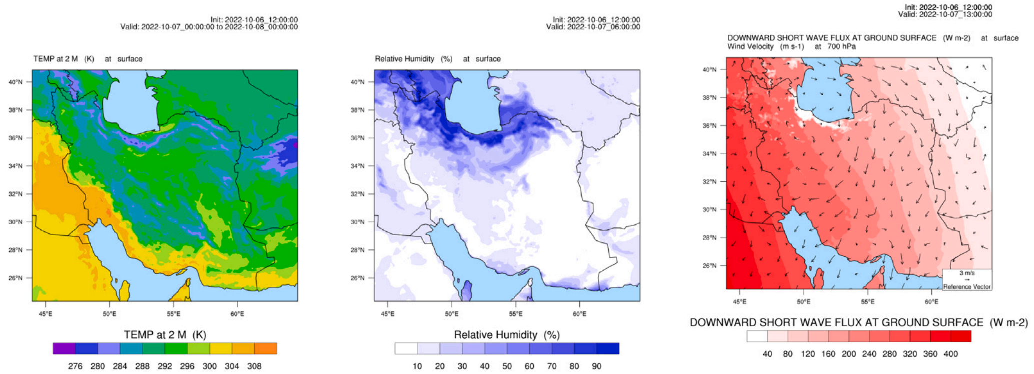

(a) Average 2m temperature (C) (b) 2m relative humidity (c) Shorwave radiation ($W.m^{-2}$) and wind speed ($m.s^{-1}$)

Fig. 3. Sample daily WRF outputs for atmospheric variables, generated by the operational forecast system, that will be ingested into the SEBAL model and ET simulations.

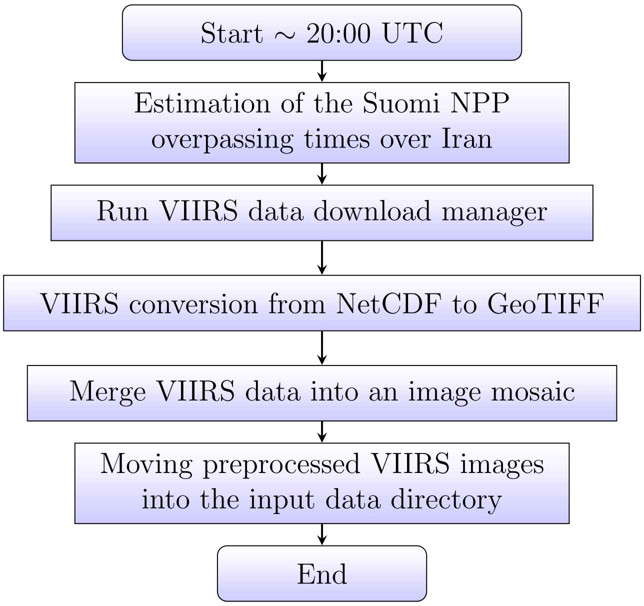

Fig. 4. Streamflow of the VIIRS data retrieval and preprocessing.

Table 3
SENTINEL2 spectral bands used by the SEBAL model.

Band	Central wavelength	Explanation	Spatial resolution
B2	0.490 μm	Blue	10 m
B3	0.560 μm	Green	10 m
B4	0.665 μm	Red	10 m
B5	0.705 μm	Vegetation red edge	20 m
B6	0.740 μm	Vegetation red edge	20 m
B7	0.783 μm	Vegetation red edge	20 m
B8	0.842 μm	Near infrared	10 m

bands, which are near infrared and red, as B8 and B4 bands, respectively.

$$NDVI := Index(NIR, RED) = \frac{NIR - RED}{NIR + RED} = \frac{B8 - B4}{B8 + B4} \tag{1}$$

Using seven bands of SENTINEL2, from B2 to B8, Albedo is calculated by Eq. (2) (Vanino et al., 2018).

$$\begin{aligned} Albedo = {} & 0.1324B2 + 0.1269B3 + 0.1051B4 + 0.0971B5 \\ & + 0.0890B6 + 0.0818B7 + 0.0722B8 \end{aligned} \tag{2}$$

Table 3 shows SENTINEL2 bands which have been used in generating 100 m Albedo and NDVI to be ingested as input data in the SEBAL model.

Unlike the VIIRS data, for the SENTINEL2 data, there is a service with special APIs to get queries and download data at specific times and regions (Access to the code at https://github.com/anikfal/GIS_solutions). With these APIs, there was no need to develop a separate module to estimate the satellite overpass time over the region. SENTINEL2 raw data can be downloaded as 110 × 110 km tiles from the online archive, in 2 different data levels of Level-1C (~600 MB) and Level-2A (~800 MB). The former data level provides the top-of-atmosphere reflectances, whereas the latter is the atmospheric corrected data for surface reflectances. At the first developmental stages of the workflow, instead of directly retrieving the Level-2A data for the bottom of the atmosphere, the Level-1C data were used to be retrieved, and then by performing the Sen2Core processor (Muller-Wilm et al., 2013), converted to the Level-2A data. The advantage of this method was reducing the download size of the SENTINEL2 data. However, in many cases, particularly when both SENTINEL2 A and B overpass Iran, the time needed to process the whole data by Sen2Core was too much that it could not be accomplished in an operational workflow in less than 24 h. Therefore, we decided to directly retrieve the Level-2A data with a larger size.

SENTINEL2 data can be retrieved in specific separate tiles, which are shown in Fig. 7(a) over the study region. Extensive regions of Iran are covered with bare dry lands, without a significant agricultural land cover. Therefore, these parts can be masked out of the study region, and not included in SENTINEL2 data retrieving and final SEBAL simulations for evapotranspiration. For this aim, those SENTINEL2 tiles in the study region that were significantly covered by bare lands were omitted from the process of data retrieval. Therefore, SENTINEL data only for those tiles shown by their centroids, which are outside of the barren lands (shaded areas in Fig. 7(a)) are retrieved. The source data to specify the barren lands has been provided by the land cover data (Buchhorn et al., 2020a) from the Copernicus Global Land Service (Buchhorn et al., 2020b).

After downloading all SENTINEL2 tiles on the simulation day, the required bands listed in Table 3 are extracted and some necessary postprocessing tasks such as conversion from digital number (DN) to reflectance (Eq. (3)) and calculation of NDVI and Albedo are carried out.

$$Reflectance = DN \div 10000 \tag{3}$$

After generating Albedo and NDVI (Fig. 7) for each tile, they are merged for SENTINEL2-A and SENTINEL2-B, separately. Regarding Figs. 7(b) and 7(c), 2 separate groups of coverage areas are distinguishable on the northwest and central parts of Iran, belonging to SENTINEL2-A and SENTINEL2-B, respectively. The latter clearly shows the selective retrieval of SENTINEL2 data for the tiles outside of the

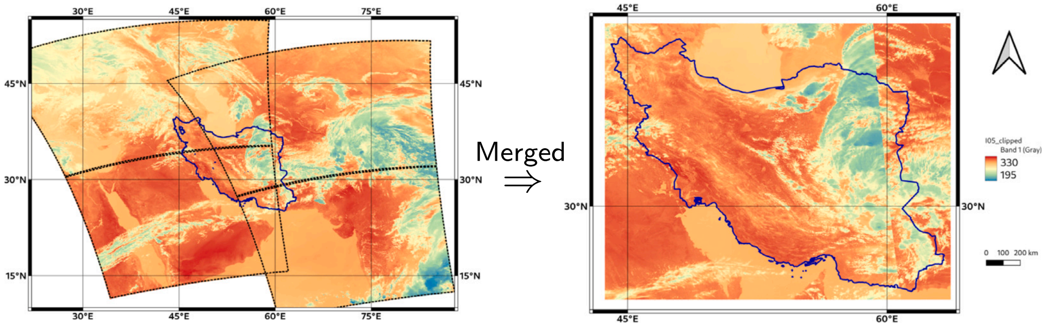

(a) VIIRS footprints over the region of study
(b) Merged and clipped VIIRS images over Iran

Fig. 5. VIIRS data retrieval and processing.

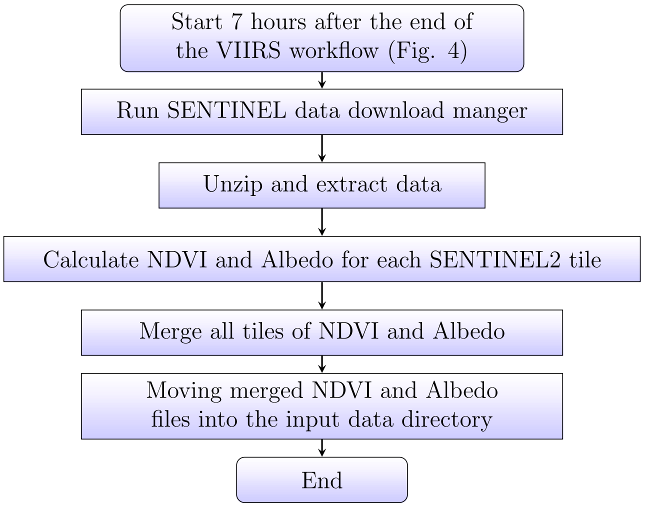

Fig. 6. Streamflow of the SENTINEL2 data retrieval and postprocessing.

barren lands. The empty areas in the same coverage area are specified as Nan values, so they will be masked and excluded in the final SEBAL simulations. Finally these parameters, besides the atmospheric variables and other supplemental input data are ingested to the SEBAL model to simulate evapotranspiration in 100 m resolution.

Estimating the best Universal Transverse Mercator (UTM) zone for the downloaded SENTINEL images is an important part of the workflow since the UTM zone must be specified before running pySEBAL for 100 m products. Iran spans over 4 UTM zones of 38, 39, 40, and 41 of the north hemisphere. Each SENTINEL2 A or B image can overpass one or two zones. However, the zone with the higher frequency of SENTINEL2 tiles (mode of the tiles' UTM zone) is set for the SEBAL model. For example, in Fig. 8, some tiles of SENTINEL2-A are shown, in which most of them (mode of tiles' zones) are in zone 40. So zone 40 will be set for the SEBAL model by the workflow. For the 375 m product, since the whole domain is considered for running of pySEBAL, the single zone 39N is set for all runs.

2.3. Static input data

In this work, the SEBAL model is not fully coupled with WRF. Therefore, Although many static surface data, including topography and soil, are included in the WRF Preprocessing System (WPS) (https://www2.mmm.ucar.edu/wrf/users/download/get_sources_wps_geog.html), it is required to provide soil and topography as static ground surface input data for the SEBAL model. WPS is a set of three programs to prepare input data for the WRF model. These programs contribute to defining model domains, extracting meteorological fields from GRIB formatted files, and horizontally interpolating the meteorological fields to model grids. The WRF static data for the aforementioned parameters cannot meet the accuracy of the spatial resolution of 375 and 100 meters in the SEBAL model. Moreover, many variables need accurate topography data to be estimated for each pixel inside the SEBAL model.

The Shuttle Radar Topography Mission (SRTM) data (Schellekens et al., 2014) with a native 30 m spatial resolution were provided as separate tiles and merged as two sets of 375 and 100 meter digital elevation model (DEM) data to be ingested in the SEBAL model. The soil data for the simulation domain was derived from the HiHydroSoil V2.0 soil maps of global hydraulic properties (Gupta et al., 2021). Soil properties that are ingested in the SEBAL model as input data are four parameters consisting of water contents at field capacity and at permanent wilting point for topsoil, and saturated water contents for topsoil (Fig. 9) and subsoil (Simons et al., 2020) - all units in m^3/m^3.

2.4. SEBAL model and the operational system

In this work, a Python implementation (pySEBAL) of the SEBAL model has been used in an operational workflow to simulate evapotranspiration as well as other daily agro-meteorological variables over the study region. The pySEBAL's codes are available from various sources. However, the main developer's code (https://github.com/TimHessels/SEBAL) has been employed in this project. The source codes of pySEBAL could be used for research case studies (single simulations). Therefore, in this work, they have been modified to be established in an operational workflow, with the capability of reading environment variables in Linux. The SEBAL model is set to run for a specific UTM zone. For the 375 m products that the SEBAL model is run for the whole simulation domain, the UTM zone is set to 39N. However, Iran spans 4 UTM zones, from 38N to 41N. For 100 m products, the best UTM zone covering the retrieved SENTINEL2 data is specified and set in the pySEBAL run variables. Therefore, for 100 m products, there are two separate runs, each for SENTINEL2 A and B.

The key element in running the original pySEBAL code is an Excel file, which must be modified by the user to address all of the requirements needed to run the model. The paths to the input data, as well as some pySEBAL internal variables, such as UTM zone and obstacle height, are stored in this Excel file in separate tabs. This Excel file is converted to a Python code, containing several classes which represent the tabs in the original Excel file and can be ingested in the workflow on an automatic operational basis. Several Linux environment variables (Table 4) are also exported at the start of the workflow to address the key paths (e.g. pySEBAL run directory and model resolution) required for the preprocessing and postprocessing tasks.

Fig. 10 shows the whole structure of the workflow of running the Python implementation of the SEBAL model in two different spatial resolutions of 375 m and 100 m. The first pySEBAL run generates the 375 m products, by incorporating the VIIRS images and WRF outputs for the required atmospheric variables. In this stage, VIIRS images after

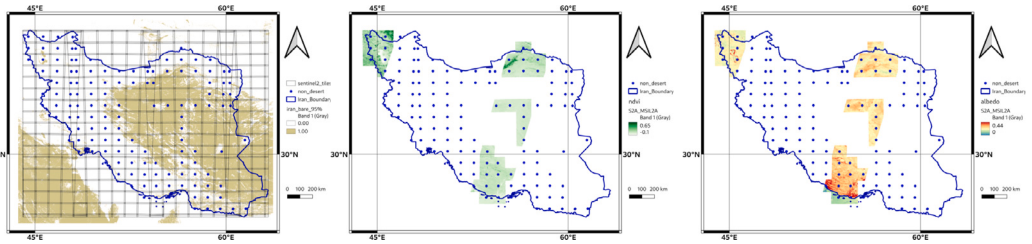

(a) Tiles outside of barren lands (b) Albedo (c) NDVI

Fig. 7. SENTINEL2 (A and B) postprocessed images for Albedo and NDVI for the tiles outside of the barren lands over the study region - July 10, 2022.

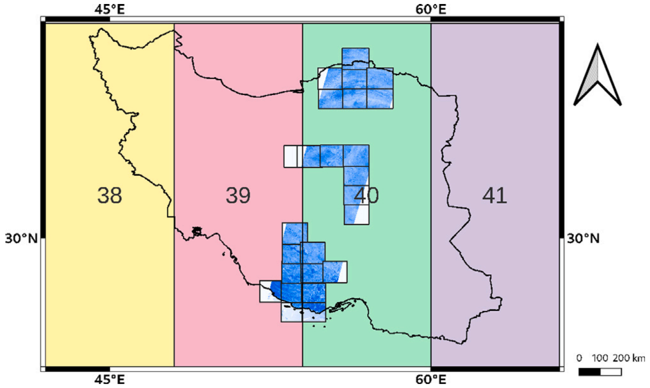

Fig. 8. UTM zones over Iran, and the locations of SENTINEL2 tiles, overpassing the region. For this case, the UTM zone 40N will be set for running pySEBAL.

Table 4
Some environment variables to control the workflow run process.

```
export wrf_processing="/home/sebal/app/wrftifs"
export wrf_output="/home/sebal/wrf/WRF/test/em_real"
export viirs_processing="/home/sebal/app/viirs_make"
export sebal_viirs_input="/home/sebal/app/sebal/Inputiran/VIIRS/"
export sebal_met_input="/home/sebal/app/sebal/Inputiran/Meteo"
export sebal_mask_file="/home/sebal/app/sebal/Inputiran/barren.tif"
export sebal_spatial_resolution="375"
export accumulated_days_period="7"
...
```

converting to GeoTIFF, without any extra postprocessing, are directly ingested into pySEBAL. The second pySEABL run to generate the 100 m products, is based on the postprocessed SENTINEL2 data as NDVI and Albedo while using the VIIRS thermal image from the previous stage of the workflow. Although the 100 m run of pySEBAL is separate from the 375 m run, if there is a problem in retrieving and preparing the VIIRS data, due to lack of the VIIRS thermal image, the 100 m run cannot be started.

Since this is an operational system, generating data and publishing the final products, even at problematic times (e.g. lacking some input data) is an important concern. For example, if the WRF model stops functioning for any reason on an arbitrary day, the system is set to use the last WRF data (likely the previous day) to run the workflow. It can be assumed that the temperature, relative humidity, and other atmospheric variables do not change too much over two consecutive days, and the values for the first day can be used by the model as input data on the second day to produce reasonable outputs.

2.5. Web service

Final pySEBAL outputs are also available via a private web portal. The website has been developed using the PHP programming language (Nixon, 2014) and Laravel web framework for back-end development. For the front-end implementation of the project, Vue.js, an open-source JavaScript framework, is used to build user interfaces and single-page applications. Additionally, the website utilizes various open-source libraries and frameworks such as Bootstrap, Font Awesome, and jQuery, as well as Nginx and Tomcat web server software. The website has two databases to store and manage production and export data. MySQL relational database is used to store and handle layer information and exported analyses, while PostgreSQL with PostGIS extension is used to store raster data and manage complicated queries for analyses.

To present geospatial data as web maps, OpenLayers, an interactive mapping service has been used. Geoserver, an open-source server application, has been employed to publish the geospatial data and allow users to access data layers through web services. Geoserver runs on the Tomcat webserver. The website has an organized structure with a header navigation menu that provides access to different sections, including *Home*, *Products*, and *Services*. The *Products* page gives an overview of various products that the website exports (pySEBAL outputs). The service page lists various services provided by the website, including point information, area analysis, comparison analysis, animation export, raster download, and reports.

2.6. Verification

The main products of this workflow, especially evapotranspiration, are usually not directly measured at meteorological stations over the study domain. So there were major limitations to access such directly measured observations. However, it was possible to verify reference evapotranspiration (ET_{ref}), as a product of the workflow, in an indirect way. Using available observational data for some meteorological variables, including temperature, pressure, humidity, and wind speed, a proper verification has been carried out to calculate ET_{ref} as observation and compare the results with the modeled ET_{ref} as a WRF/SEBAL product.

Regarding the availability of observation data, we investigated the study domain to select a couple of days with the least cloud cover. The EUMETView service (https://view.eumetsat.int) and its dust RGB product (with good identification of clouds) have been used to specify 4 days of April 15, May 30, June 17, and June 25 of the year 2021, with no or little cloudiness over Iran. Then the workflow has been manually run for these four days to generate the products (modeled outputs), including ET_{ref}. Then, the values of ET_{ref} have been simulated using the observations (weather station data) for some locations, specified in Fig. 9.

The atmospheric variables over the locations in Fig. 9 have been provided from the national meteorological stations, in the four specified days. Using an NCL code (available at https://github.com/anikfal/atmospheric_science) and these observations, ET_{ref} has been calculated for each location, to be considered as observational ET_{ref}. Required input data for calculating ET_{ref} are as follows: the Julian day of the simulation date, latitude and elevation of the weather station, air pressure, wind speed, maximum and minimum temperature, maximum and minimum relative humidity, and if measured, daylight sun hours

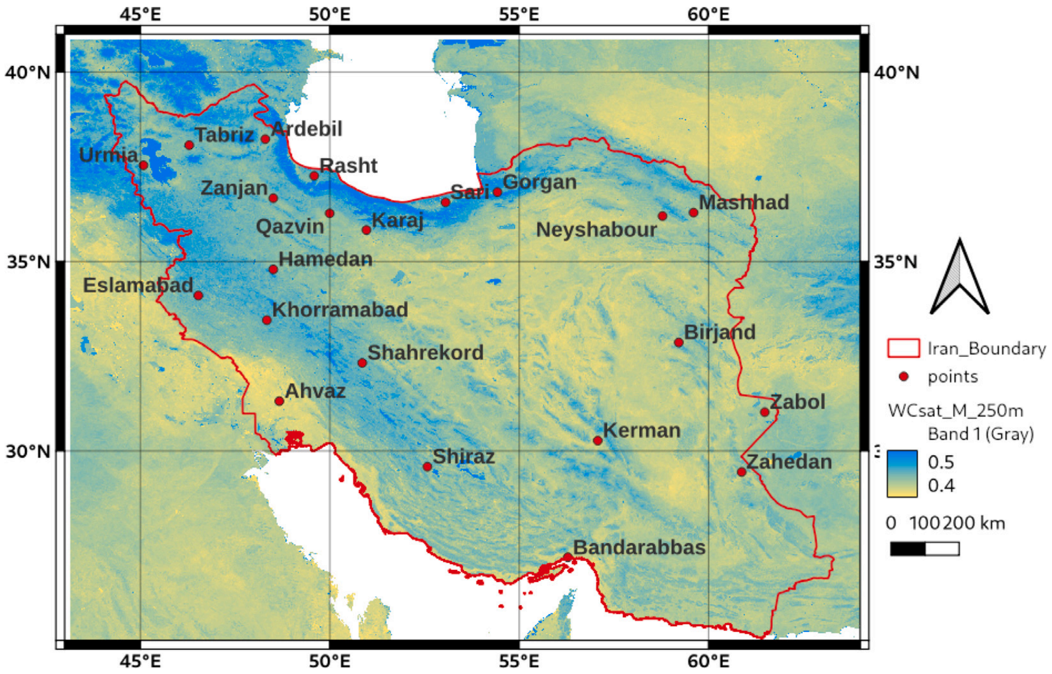

Fig. 9. Topsoil saturated water content (m^3/m^3) from the Hihydrosoil global data, overlaid by the selected locations used in the verification process.

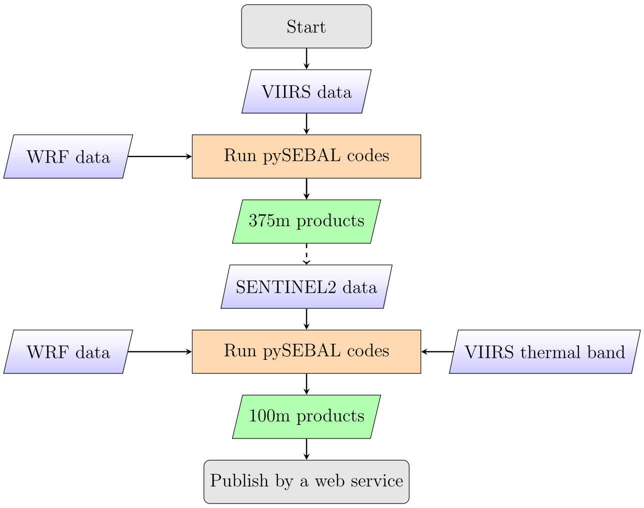

Fig. 10. Overall workflow for the 375 m and 100 m SEBAL products.

and Albedo at the weather station. Fig. 11 shows the relationship between the modeled and calculated (observed) ET_{ref} in four scatter plots as a display of the performance of the WRF/SEBAL workflow.

According to Fig. 11, the variation in ET_{ref} with regard to different dates in the year has been reasonably modeled by the WRF/SEBAL workflow. So the gradual increase in the calculated ET_{ref} from April to June is consistent and in line with the gradual increase in the modeled ET_{ref}. The RMSEs between modeled and observed ET_{ref} in June are showing higher values. Higher errors in case of higher values of ET_{ref} can be expected, assuming that the errors are proportional to the size of the modeled outputs. The RMSEe indicates values more or less than 2 mm/day. Although the size of such RMSEs is reasonable for evapotranspiration, it may not be the best accuracy and performance for a model output. However, the WRF/SEBAL is mainly not based on statistical approaches and this accuracy for such a complex operational system with outputs for a whole country area, can be quite reasonable.

3. Results

SEBAL outputs are generated in two sets of 375 m and 100 m GeoTIFF files. The 100 m outputs can consist of two separate groups, in case both the SENTINEL2-A and SENTINEL2-B data are retrieved. Overall, the size of the generated data plus all input data at most, can reach 100 Gigabytes per day, with more than half of them coming from SENTINEL2 data. The workflow usually ends in the early morning, before 06:00 am. The number of final products is almost the same for both 100 m and 375 m outputs.

Fig. 12 shows the main pySEBAL outputs which are classified and stored in distinguished directories (green highlights). Some of the pySEBAL's outputs are input data that are mapped and resampled on the SEBAL simulation domain. For example, atmospheric input data, as well as satellite reflectance in different bands are also stored as output data in GeoTIFF format, in their associated directories. FPAR is the abbreviation for the fraction of Photosynthetically active radiation (PAR) absorbed by the vegetation canopy, estimated as a function of NDVI (Eq. (4)).

$$FPAR = -0.161 + 1.257 \times NDVI \tag{4}$$

Among all SEBAL outputs, some important outputs are kept and postprocessed by the operational system, and the rest of the outputs are removed.

Fig. 13 shows the 375 m products for the actual and potential evapotranspirations. Each output is a clipped image of the original SEBAL outputs by Iran's border. Higher values of potential ET in the bottom row images can be clearly distinguished from those of the upper row images of the actual ET. High values of ET around the southern coast of the Caspian Sea which is covered by dense vegetation (farms and forests), can be distinguished among other regions of the study area. Overall, the actual ET values (Figs. 13(a) and 13(b)) in May are larger than those (Figs. 13(c) and 13(d)) in June 2022, which is dryer with lower NDVI. The algorithm of pySEBAL is capable of identifying the clouds and their shades, based on a simple NDVI and the satellite's data quality maps. Therefore, cloudy areas are masked in the simulation region. Regarding Fig. 13(c), the white regions in the western parts of Iran are masked as cloudy, and the white regions in the eastern and central parts are barren (desert) regions, which are masked as well.

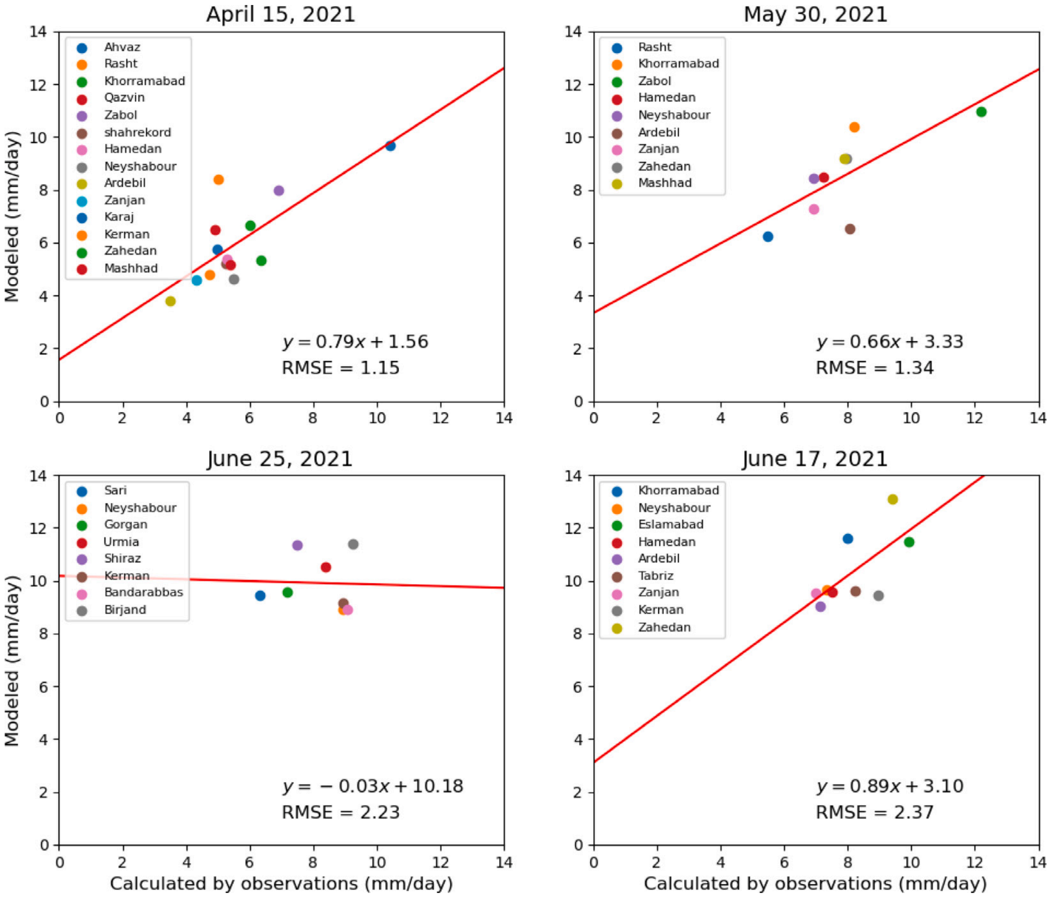

Fig. 11. Scatter plots of the modeled ET_{ref} (Y axes) as the output of the WRF/SEBAL system, and calculated ET_{ref} (X axes) using observation data, in four different days.

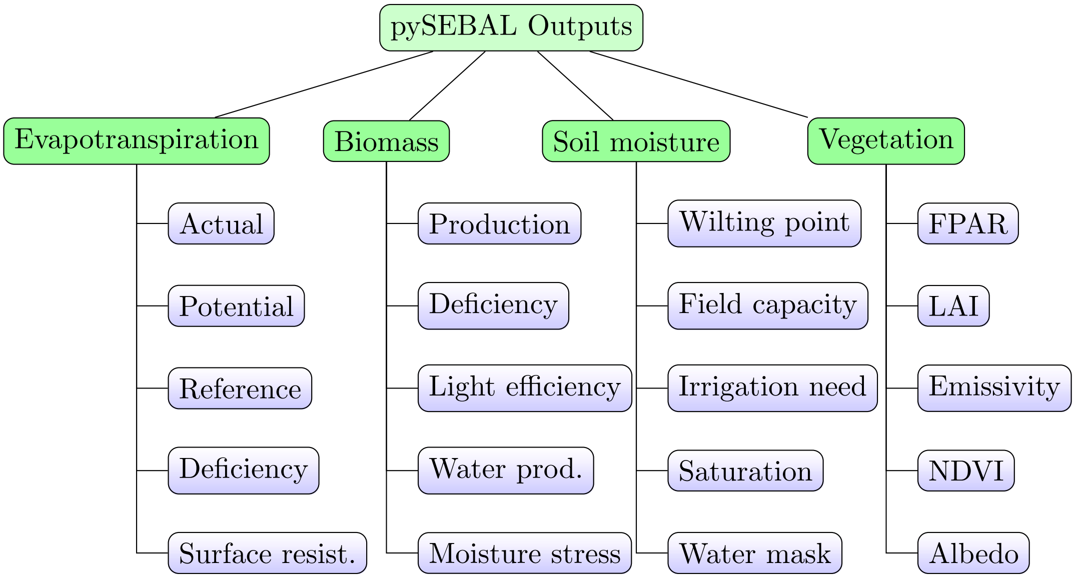

Fig. 12. Main output products of pySEBAL.

Figs. 13, 14, and 15 are simulated in dates with the least cloud covers, particularly over northern and south-western Iran. Fig. 14 shows the 100 m products for the actual and potential evapotranspirations. Regarding the actual evapotranspiration maps (Figs. 14(a) to 14(d)), each image is based on one of the SENTINEL-2 (A or B) footprints, that together cover the whole region every 5 days. In all images, but the images in the first column, two swaths are shown, which are associated with SENTINEL2 A and B. However, Figs. 14(a) and 14(e) are demonstrated with only one swath, covering central parts of Iran. Missing values in each image are either due to barren lands, or cloud masks. Tiles of the SENTINEL2 satellites can be clearly distinguished in the second column of Fig. 14 (Figs. 14(b) and 14(f)). Furthermore, a missing tile can be identified in the second-column images. The region associated with the missing tile was not a barren land, but

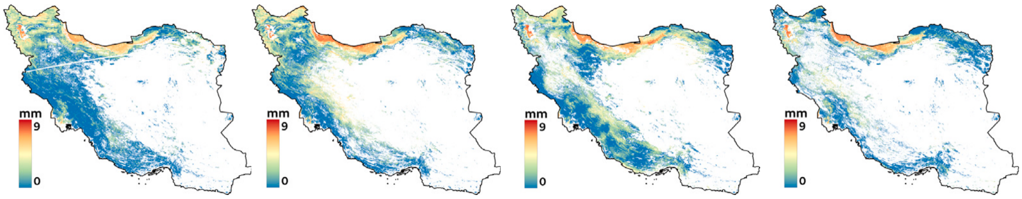

(a) ET_{act} - May 19 (b) ET_{act} - May 30 (c) ET_{act} - June 17 (d) ET_{act} - June 25

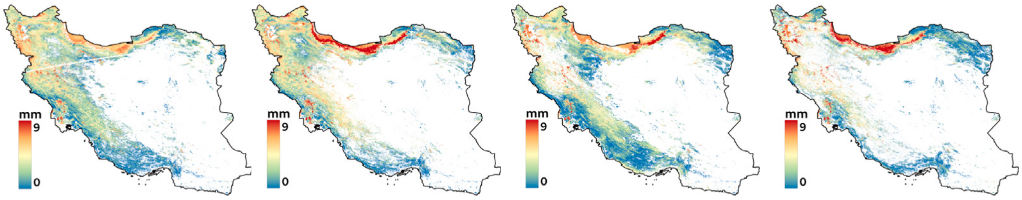

(e) ET_{pot} - May 19 (f) ET_{pot} - May 30 (g) ET_{pot} - June 17 (h) ET_{pot} - June 25

Fig. 13. 375 m outputs for actual (upper row) and potential (bottom row) evapotranspiration in year 2021.

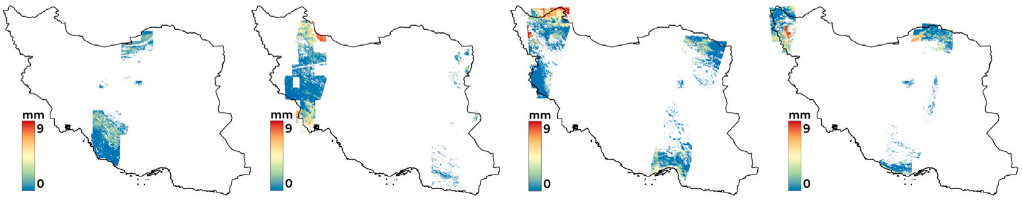

(a) ET_{act} - May 19 (b) ET_{act} - May 30 (c) ET_{act} - June 17 (d) ET_{act} - June 25

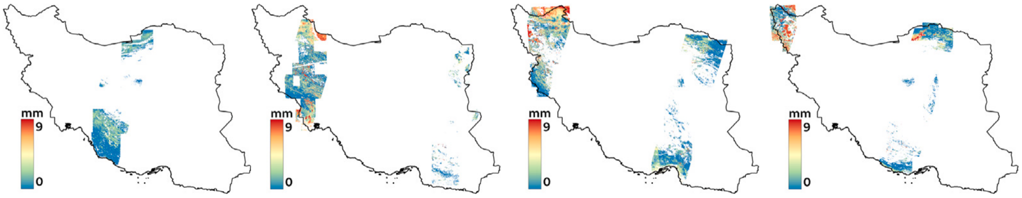

(e) ET_{pot} - May 19 (f) ET_{pot} - May 30 (g) ET_{pot} - June 17 (h) ET_{pot} - June 25

Fig. 14. 100 m outputs for actual (upper row) and potential (bottom row) evapotranspiration in year 2021.

due to some data retrieval failure, the SENTINEL2 tile, as one of the input data (besides atmospheric, static, and thermal band data) could not be downloaded, and therefore, that region was incorporated as missing values in the SEBAL final simulation. SENTINEL2 and VIIRS data retrieval failures happen regularly once or twice a month in the operational system, and the reason is still unknown. In some cases, SENTINEL2 data retrieval failure can occur in a way that no tiles are downloaded and therefore, no 100 m product will be generated.

Fig. 15 shows the biomass production as a main output of the SEBAL model. Biomass production is a function of absorbed photosynthetically active radiation (APAR) and light use efficiency (LUE), that are calculated in pySEBAL (Eq. (5)).

$$Biomass\ Procution = APAR \times LUE \times 0.864 \tag{5}$$

Similarities in the spatial variations of the biomass production with those of Evapotranspiration can be identified by comparing Fig. 15 with Figs. 13 and 14, especially in northern Iran with high ET values, that can reach to more than 100 kg ha^{-1} day^{-1}. It should be noted that vast regions of northern Iran with high biomass production values are covered by forests, and are not considered as crop fields. To have pySEBAL outputs for the warm climate of southern Iran, it was required to increase the upper limit of stomatal activity to 45 degrees. Otherwise, the areas with higher temperatures will be masked in the outputs. Especially west southern parts of Iran (Fig. 16) as a flat low-altitude region, regularly exceeds 40 degrees from the middle of spring to the end of summer.

Outputs of the operational system for the year 2022 have been stored as an archived dataset. To show the time series of the variations of some important products, including biomass and evapotranspiration, biomass production of a specific region of sugarcane farms in southwest of Iran, in 30'rd of May has been investigated. This region is usually with low cloudiness, so it is an appropriate study field to investigate the time series of the simulated ET and biomass. To distinguish and specify sugarcane pixels, values of biomass production greater than 35 kg ha^{-1} day^{-1} have been extracted from the region (Fig. 16). These pixels have been used as fixed locations to extract the time series of actual and potential evapotranspiration, albedo, leaf area index (as a surrogate of NDVI), and biomass production itself. Average values of the extracted pixels have been plotted as time series diagrams to determine the variations of the primary products of the operational system from February 2022 to January 2023.

Fig. 17(a) shows the time series of the average values of the actual and potential ET over sugarcane farms, delineated in Fig. 16. Potential ET values show distinguished differences from those of the actual ET, from May to November. Maximum ET values in July and August are consistent with the high sugarcane growth rate in such period (Hamdi, 2016). The difference between actual and potential ET is also maximum in this period. Most rainfall occurs between November and April, the coolest months in the region, which shows the least differences between the actual and potential ET.

Fig. 17(b) shows the time series of the variations of LAI and Albedo for the same sugarcane fields. The values of LAI almost follow the

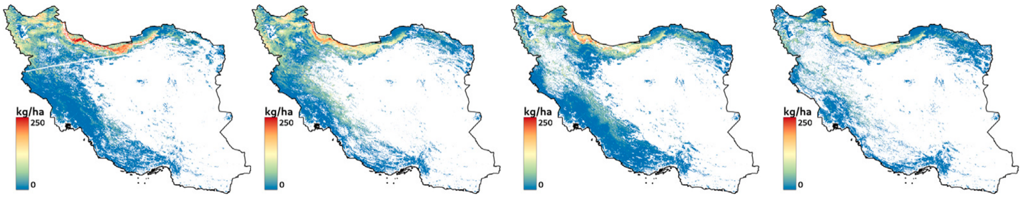

(a) ET_{act} - May 19 (b) ET_{act} - May 30 (c) ET_{act} - June 17 (d) ET_{act} - June 25

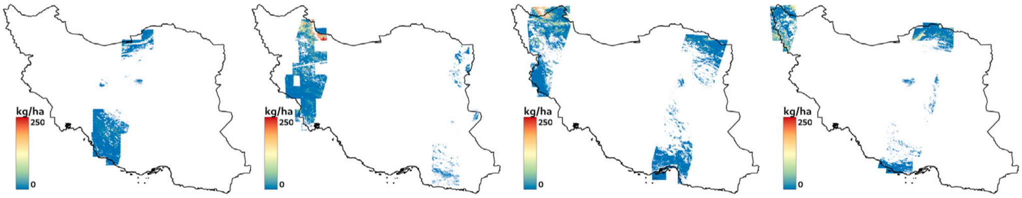

(e) ET_{pot} - May 19 (f) ET_{pot} - May 30 (g) ET_{pot} - June 17 (h) ET_{pot} - June 25

Fig. 15. Biomass production (kg/ha) for 375 m (upper row) and 100 m (bottom row) products in year 2021.

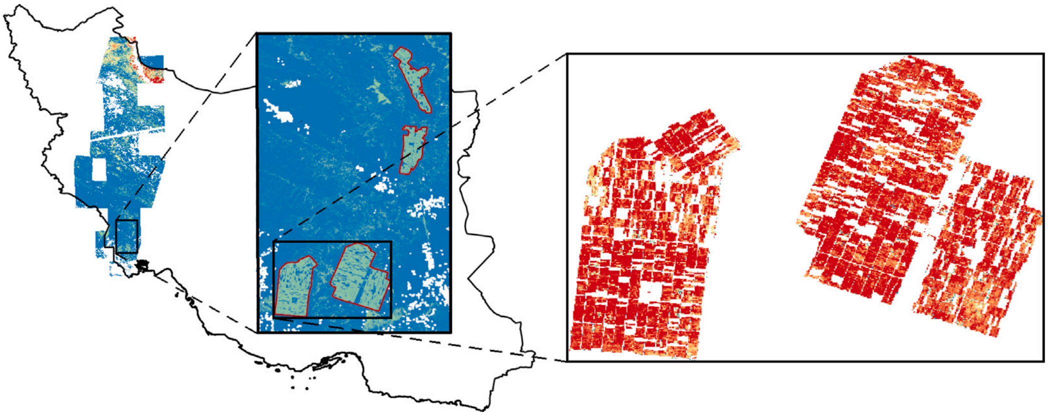

Fig. 16. Extraction of the pixel locations for the sugarcane fields, from 100 m products.

same pattern as that of evapotranspiration (Fig. 17(a)). However, a lag between the maximum values for these LAI and ET can be noticed. Therefore, according to the time series, LAI (NDVI) values reach their maximum, about 1 month after the time of maximum evapotranspiration. The Albedo values almost show a uniform pattern through the time series. The time series for the biomass production in Fig. 17(c) is quite non-uniform, with a lot of variations. However, a rise in the diagram can be noticed from July onward, which is more or less consistent with the rise in Albedo in Fig. 17(b). Particularly, for the sugarcane in this region, cultivation usually starts around July, which meets the time series of the biomass variations.

There can be seen some outlier values in the beginning and end of the diagram. These outliers in Albedo are mostly due to the failure of pySEBAL in distinguishing the cloud cover and therefore, applying the cloud mask. Therefore, for some regions, the cloud-covered areas with high Albedo are not masked and are included in the final products with erroneous outputs. Sources of errors are more than the failure in cloud detection. Many parameters and key variables used in the simulation of ET and the associated products are estimated by applying the DEM in the simulations. There are also many assumptions such as grass height that cannot be considered separately for each crop and are set as a single value for the whole simulation domain.

4. Discussions

The workflow discussed in this article is the first water management system for the region that is fully based on operational sectors, consisting of numerical weather forecasting, satellite data retrieval and processing, and hydrological simulations, in a High Performance Computing (HPC) system. This system provides daily evapotranspiration, biomass products, as well as other relevant agrometeorological variables for the domain of simulation (Iran). The provision of such a system for a region with high rates of evapotranspiration is of paramount importance for mechanized and efficient cultivation and agricultural management. The combination of a regional weather model with satellite images to provide input data operationally for the final simulation was a complex workflow to make some atmospheric and land variables that have a significant impact on agricultural water management and the final crop yield. 375 m products cover the whole domain and provide daily outputs. Whereas, 100 m products are not available every day, but every 5 days for a specific point. Therefore, 375 m products have higher temporal, and lower spatial resolutions in comparison to 100 m products.

The output products are also available as a private web service. However, this service can be developed to be a warning advisory system, by defining some thresholds in moisture stress, wilting point, and other associated variables with the water stress and irrigation need. The system can be used for different purposes, besides agriculture. For example, detecting high actual evapotranspiration pixels in regions that are not near water sources and are not expected to have high values in actual ET, can be determined as exploiting an underground water source, which can be a new drilled well. Furthermore, outputs of the operational water management systems are supposed to be stored as long-term data archives. Therefore, such a dataset will be a valuable resource for environmental scientists and agricultural experts to study the hydrological cycle of the region.

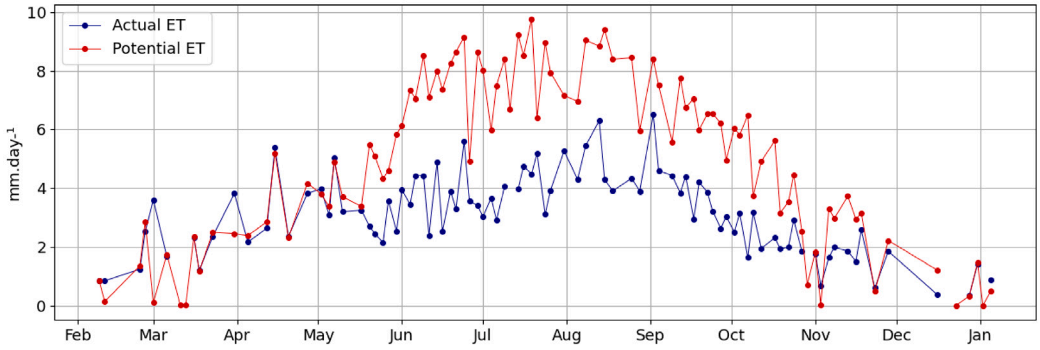

(a) Actual and potential ET (mm.day^{-1})

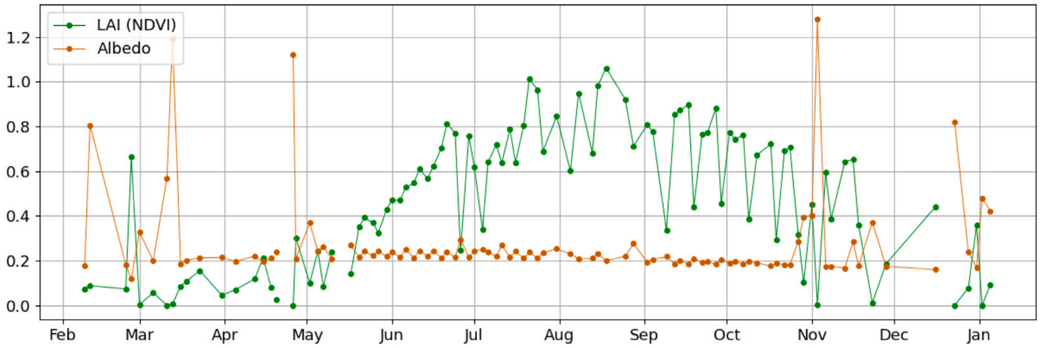

(b) Albedo, and Leaf Area Index (∼ NDVI)

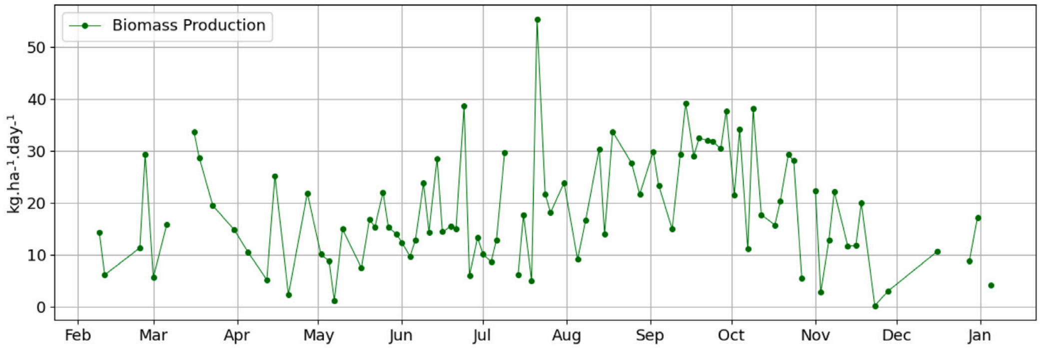

(c) Biomass production (kg.ha^{-1}.day^{-1})

Fig. 17. Daily time series of the average values of actual and potential ET and biomass production from February 2022 to January 2023, over the pixels specified in Fig. 16.

One of the primary deficiencies of the WRF/SEBAL system is the spatial and temporal inconsistencies between the input data provided by different satellites and the WRF model, which can have an impact on the accuracy of final products. Some of these deficiencies are handled inside pySEBAL, such as sharpening the thermal band retrieved from the VIIRS sensor, by using the ALBEDO values from SENTINEL2 data. However, more advanced methodologies, including artificial intelligence can take part to handle such challenges more effectively. Furthermore, the WRF/SEBAL system can be managed to be run for separate small domains with very high spatial resolution (based on the 10 m SENTINEL2 data). Running the WRF/SEBAL system by such a high resolution configuration is quite not possible by regular HPC systems. However, such a 10 m resolution workflow can provide products for several small domains. For each domain, the WRF model can also be configured to be run by high resolution grids (1 km or less).

Due to various components in the operational workflow, including the preprocessing and postprocessing stages, the accuracy of the final products may not reach that of the statistical models for specific geographical locations, especially if such statistical models are based on observation input data. However, some outstanding features make this operational system distinguished. The most important ones are its coverage for a whole region or country, with outputs on a regular grid, its daily simulated products, and the point that such a workflow is a fully software-based system, without any special device or field requirements.

5. Conclusions

The WRF/SEBAL operational system can be developed to address more details and requirements in association with water management, farming, and even applications like irrigation prediction that depend on weather forecasts. The forecast time of the WRF model in the current operational system can be extended to give forecasts for a couple of days. Therefore, atmospheric forecasts can also provided as additional products. The WRF model can play a much more profound role in the developed version of this system, rather than just providing a couple of atmospheric input variables to the SEBAL model. One of the primary challenges of pySEBAL is masking cloud cover. The accuracy of the mask algorithm is a primary issue, but the masked areas that are empty in the final products are also a concern, that can be handled by replacing the relevant variables calculated by the satellite data (such as the thermal band) with those simulated by the WRF model.

Such an operational system can be established with enhanced configurations and better performance for smaller regions. In other words, if the region is small, it will be less required to merge the retrieved satellite data to be ingested as the input data into the final SEBAL model. Moreover, small regions are more likely to be inside a whole UTM zone, which is a convenient condition for the SEBAL model. SEBAL model uses some empirical algorithms to estimate evapotranspiration and its associated parameters. These algorithms can be revisited and calibrated against the observation data in the study domain, to reach a higher simulation accuracy.

CRediT authorship contribution statement

Amirhossein Nikfal: Writing – review & editing, Writing – original draft, Visualization, Validation, Supervision, Software, Resources, Methodology, Investigation, Formal analysis, Data curation, Conceptualization. **Mohammad Amin Karimi:** Writing – original draft, Software, Methodology, Data curation.

Declaration of competing interest

The authors declare that they have no known competing financial interests or personal relationships that could have appeared to influence the work reported in this paper.

Data availability

Many data, models, and codes in this work are opensource. However, the final outputs are not available to public, but can be sent to interested researchers.

Acknowledgments

We would like to thank Dr. Majid Vazifedoust, the faculty member of the University of Guilan, for his role in the methodology of this work.

We also thank Ms. Masoumeh Khorani for her technical contribution to the OpenLayers web map service for the products.

References

Alizadeh, A., Keshavarz, A., 2005. Status of agricultural water use in Iran. In: Water Conservation, Reuse, and Recycling: Proceedings of an Iranian-American Workshop. Vol. 4, National Academies Press Washington DC, USA, pp. 94–105.

Bastiaanssen, W.G., Menenti, M., Feddes, R., Holtslag, A., 1998a. A remote sensing surface energy balance algorithm for land (SEBAL). 1. Formulation. J. Hydrol. 212, 198–212.

Bastiaanssen, W.G., Pelgrum, H., Wang, J., Ma, Y., Moreno, J., Roerink, G., Van der Wal, T., 1998b. A remote sensing surface energy balance algorithm for land (SEBAL).: Part 2: Validation. J. Hydrol. 212, 213–229.

Brenner, C., Zeeman, M., Bernhardt, M., Schulz, K., 2018. Estimation of evapotranspiration of temperate grassland based on high-resolution thermal and visible range imagery from unmanned aerial systems. Int. J. Remote Sens. 39 (15–16), 5141–5174.

Buchhorn, M., Lesiv, M., Tsendbazar, N.-E., Herold, M., Bertels, L., Smets, B., 2020a. Copernicus global land cover layers—collection 2. Remote Sens. 12 (6), 1044.

Buchhorn, M., Smets, B., Bertels, L., De Roo, B., Lesiv, M., Tsendbazar, N.-E., Herold, M., Fritz, S., 2020b. Copernicus global land service: Land cover 100m: collection 3: epoch 2019: Globe. Version V3. 0.1.

Caiserman, A., Amiraslani, F., Dumas, D., 2021. Assessment of the agricultural water budget in southern Iran using Sentinel-2 to Landsat-8 datasets. J. Arid Environ. 188, 104461.

Cao, C., Xiong, J., Blonski, S., Liu, Q., Uprety, S., Shao, X., Bai, Y., Weng, F., 2013. Suomi NPP VIIRS sensor data record verification, validation, and long-term performance monitoring. J. Geophys. Res.: Atmos. 118 (20), 11–664.

Droogers, P., Immerzeel, W., Lorite, I., 2010. Estimating actual irrigation application by remotely sensed evapotranspiration observations. Agricult. Water Manag. 97 (9), 1351–1359.

Drusch, M., Del Bello, U., Carlier, S., Colin, O., Fernandez, V., Gascon, F., Hoersch, B., Isola, C., Laberinti, P., Martimort, P., et al., 2012. Sentinel-2: ESA's optical high-resolution mission for GMES operational services. Remote Sens. Environ. 120, 25–36.

Ellsäßer, F., Röll, A., Stiegler, C., Hölscher, D., et al., 2020. Introducing qWaterModel, a QGIS plugin for predicting evapotranspiration from land surface temperatures. Environ. Model. Softw. 130, 104739.

Falk, M., Pyles, R., Ustin, S., Xu, L., Whiting, M., Sanden, B., Brown, P., et al., 2014. Evaluated crop evapotranspiration over a region of irrigated orchards with the improved ACASA–WRF model. J. Hydrometeorol. 15 (2), 744–758.

Goyal, M.R., Harmsen, E.W., 2013. Evapotranspiration: Principles and Applications for Water Management. CRC Press.

Gupta, S., Lehmann, P., Bonetti, S., Papritz, A., Or, D., 2021. Global prediction of soil saturated hydraulic conductivity using random forest in a covariate-based geotransfer function (CoGTF) framework. J. Adv. Modelling Earth Syst. 13 (4), e2020MS002242.

Hamdi, H., 2016. Sustainability in sugarcane production: opportunities and limitations in Southwest of Iran. Sugar Tech 18 (6), 642–646.

Hong, M., Lee, S.-H., Lee, S.-J., Choi, J.-Y., 2021. Application of high-resolution meteorological data from NCAM-WRF to characterize agricultural drought in small-scale farmlands based on soil moisture deficit. Agricult. Water Manag. 243, 106494.

Karimi, V., Karami, E., Keshavarz, M., 2018. Climate change and agriculture: Impacts and adaptive responses in Iran. J. Integr. Agric. 17 (1), 1–15.

Kool, D., Agam, N., Lazarovitch, N., Heitman, J., Sauer, T., Ben-Gal, A., 2014. A review of approaches for evapotranspiration partitioning. Agricult. Forest Meterol. 184, 56–70.

Lu, J., Carbone, G.J., Huang, X., Lackstrom, K., Gao, P., 2020. Mapping the sensitivity of agriculture to drought and estimating the effect of irrigation in the United States, 1950–2016. Agricult. Forest Meteorol. 292, 108124.

Madani, K., 2014. Water management in Iran: what is causing the looming crisis? J. Environ. Stud. Sci. 4, 315–328.

Mhawej, M., Faour, G., 2020. Open-source google earth engine 30-m evapotranspiration rates retrieval: The SEBALIGEE system. Environ. Model. Softw. 133, 104845.

Mo, X., Liu, S., Lin, Z., Zhao, W., 2004. Simulating temporal and spatial variation of evapotranspiration over the Lushi basin. J. Hydrol. 285 (1–4), 125–142.

Muller-Wilm, U., Louis, J., Richter, R., Gascon, F., Niezette, M., 2013. Sentinel-2 level 2A prototype processor: Architecture, algorithms and first results. In: Proceedings of the ESA Living Planet Symposium, Edinburgh, UK. pp. 9–13.

Narasimhan, B., Srinivasan, R., 2005. Development and evaluation of Soil Moisture Deficit Index (SMDI) and Evapotranspiration Deficit Index (ETDI) for agricultural drought monitoring. Agricult. Forest Meterol. 133 (1–4), 69–88.

Nikfal, A., 2023. PostWRF: Interactive tools for the visualization of the WRF and ERA5 model outputs. Environ. Model. Softw. 160, 105591.

Nixon, R., 2014. Learning PHP, MySQL & JavaScript: With jQuery, CSS & HTML5. " O'Reilly Media, Inc.".

Petropoulos, G.P., Ireland, G., Lamine, S., Griffiths, H.M., Ghilain, N., Anagnostopoulos, V., North, M.R., Srivastava, P.K., Georgopoulou, H., 2016. Operational evapotranspiration estimates from SEVIRI in support of sustainable water management. Int. J. Appl. Earth Obs. Geoinf. 49, 175–187.

Pyles, R.D., 2000. The Development and Testing of the UCD Advanced Canopy-Atmosphere-Soil Algorithm (ACASA) for Use in Climate Prediction and Field Studies. University of California, Davis.

QGIS Development Team, 2020. QGIS Geographic Information System. QGIS Association.

Rind, D., Goldberg, R., Hansen, J., Rosenzweig, C., Ruedy, R., 1990. Potential evapotranspiration and the likelihood of future drought. J. Geophys. Res.: Atmos. 95 (D7), 9983–10004.

Schellekens, J., Brolsma, R., Dahm, R., Donchyts, G., Winsemius, H., 2014. Rapid setup of hydrological and hydraulic models using OpenStreetMap and the SRTM derived digital elevation model. Environ. Model. Softw. 61, 98–105.

Simons, G., Koster, R., Droogers, P., 2020. Hihydrosoil V2. 0-High Resolution Soil Maps of Global Hydraulic Properties. Wageningen, The Netherlands, [online] Available from: https://www.futurewater.nl/wpcontent/uploads/2020/10/HiHydroSoil-v2.0-High-Resolution-Soil-Maps-of-Global-Hydraulic-Properties.pdf.

Skamarock, W.C., Klemp, J.B., Dudhia, J., Gill, D.O., Liu, Z., Berner, J., Wang, W., Powers, J.G., Duda, M.G., Barker, D.M., et al., 2019. A description of the advanced research WRF model version 4. Natl. Center Atmos. Res. 145 (145), 550, Boulder, CO, USA.

Sun, S., Ouyang, S., Hu, Y., Zhao, Z., Liu, M., Chen, L., Zeng, Y., Peng, C., Zhou, X., Xiang, W., 2023. rTRIPLEXCWFlux: An r package for carbon–water coupling model to simulate net ecosystem productivity and evapotranspiration in forests. Environ. Model. Softw. 162, 105661.

Sun, Z., Wei, B., Su, W., Shen, W., Wang, C., You, D., Liu, Z., 2011. Evapotranspiration estimation based on the SEBAL model in the nansi lake wetland of China. Math. Comput. Modelling 54 (3–4), 1086–1092.

Tang, R., Li, Z.-L., Chen, K.-S., Jia, Y., Li, C., Sun, X., 2013. Spatial-scale effect on the SEBAL model for evapotranspiration estimation using remote sensing data. Agricult. Forest Meterol. 174, 28–42.

Teuling, A.J., Van Loon, A.F., Seneviratne, S.I., Lehner, I., Aubinet, M., Heinesch, B., Bernhofer, C., Grünwald, T., Prasse, H., Spank, U., 2013. Evapotranspiration amplifies European summer drought. Geophys. Res. Lett. 40 (10), 2071–2075.

Theron, S., Archer, E., Midgley, S., Walker, S., 2021. Agricultural perspectives on the 2015–2018 western cape drought, south Africa: Characteristics and spatial variability in the core wheat growing regions. Agricult. Forest Meteorol. 304, 108405.

Tsakiris, G., Vangelis, H., 2005. Establishing a drought index incorporating evapotranspiration. Eur. Water 9 (10), 3–11.

Vanino, S., Nino, P., De Michele, C., Bolognesi, S.F., D'Urso, G., Di Bene, C., Pennelli, B., Vuolo, F., Farina, R., Pulighe, G., et al., 2018. Capability of sentinel-2 data for estimating maximum evapotranspiration and irrigation requirements for tomato crop in central Italy. Remote Sens. Environ. 215, 452–470.

Xiang, K., Li, Y., Horton, R., Feng, H., 2020. Similarity and difference of potential evapotranspiration and reference crop evapotranspiration–a review. Agricult. Water Manag. 232, 106043.

Xue, J., Bali, K.M., Light, S., Hessels, T., Kisekka, I., 2020. Evaluation of remote sensing-based evapotranspiration models against surface renewal in almonds, tomatoes and maize. Agricult. Water Manag. 238, 106228.

Zarafshani, K., Sharafi, L., Azadi, H., Hosseininia, G., De Maeyer, P., Witlox, F., 2012. Drought vulnerability assessment: The case of wheat farmers in Western Iran. Glob. Planet. Change 98, 122–130.

Zhang, K., Kimball, J.S., Running, S.W., 2016. A review of remote sensing based actual evapotranspiration estimation. Wiley Interdiscip. Rev.: Water 3 (6), 834–853.